Plasmonic Pt Superstructures with Boosted Near-Infrared Absorption and Photothermal Conversion Efficiency in the Second Biowindow for Cancer Therapy

Qishun Wang, Huan Wang, Yang Yang,* Longhai Jin, Yang Liu, Ying Wang, Xiangyu Yan, Jing Xu, Ruoqian Gao, Pengpeng Lei, Junjie Zhu, Yinghui Wang,* Shuyan Song,* and Hongjie Zhang

Photothermal therapy triggered by near-infrared light in the second biowindow (NIR-II) has attracted extensive interest owing to its deeper penetration depth of biological tissue, lower photon scattering, and higher maximum permissible exposure. In spite of noble metals showing great potential as the photothermal agents due to the tunable localized surface plasmon resonance, the biological applications of platinum are rarely explored. Herein, a monocomponent hollow Pt nanoframe ("Pt Spirals"), whose superstructure is assembled with three levels (3D frame, 2D layered shells, and 1D nanowires), is reported. Pt Spirals exhibit outstanding photothermal conversion efficiency (52.5%) and molar extinction coefficients (228.7 m^2 mol^{-1}) in NIR-II, which are much higher than those of solid Pt cubes. Simulations indicate that the unique superstructure can be a significant cause for improving both adsorption and the photothermal effect simultaneously in NIR-II. The excellent photothermal effect is achieved and subsequently verified in in vitro and in vivo experiments, along with superb heat-resistance properties, excellent photostability, and a prominent effect on computed tomography (CT) imaging, demonstrating that Pt Spirals are promising as effective theranostic platforms for CT imaging-guided photothermal therapy.

Photothermal therapy (PTT) based on near-infrared (NIR) light induced local hyperthermia for ablating tumors has aroused significant interest owing to its noninvasiveness, high

temporal, and spatial controllability, and minimized adverse side effects. Research into developing nanomaterials as photothermal agents has bloomed in the past few years, such as noble metal nanostructures,[1–12] main group metal,[13] transition metal chalcogenides,[14–24] carbon nanomaterials,[25–28] organic/bioorganic materials,[29–31] and so on. However, the most widely used excitation lights in PTT are mainly located in the first near-infrared biowindow (NIR-I, 700–1000 nm), which has a low maximum permissible exposure (MPE, 0.33 W cm^{-2} at 808 nm according to ANSI Z136.1-2014, American National Standard for Safe Use of Lasers) for skin exposure, resulting in limited application in cancer clinical therapy. Comparatively, the light in the second near-infrared biowindow (NIR-II, 1000–1350 nm) has a deeper penetration depth of biological tissue, lower photon scattering, and higher MPE (1.0 W cm^{-2}), indicating that it is more suitable for PTT.[32] Therefore, it is highly desired to explore novel photothermal agents with high absorption and photothermal conversion efficiency (PCE, η) in NIR-II.

Q. Wang, Dr. Y. Yang, Dr. J. Zhu
Department of Thoracic Surgery
Shanghai Pulmonary Hospital
Tongji University
Shanghai 200433, P. R. China
E-mail: timyangsh@tongji.edu.cn
Q. Wang, H. Wang, Y. Liu, Y. Wang, J. Xu, Dr. P. Lei, Dr. Y. Wang,
Prof. S. Song, Prof. H. Zhang
State Key Laboratory of Rare Earth Resource Utilization
Changchun Institute of Applied Chemistry
Chinese Academy of Sciences
Changchun, Jilin 130022, P. R. China
E-mail: yhwang@ciac.ac.cn; songsy@ciac.ac.cn

Dr. L. Jin
Department of Radiology
The Second Hospital of Jilin University
Changchun 130041, P. R. China

X. Yan
Jilin Changyu Advanced Materials Company
Changchun 130000, P. R. China

R. Gao
Changchun Institute of Optics, Fine Mechanics and Physics
Chinese Academy of Sciences
Changchun 130033, P. R. China

**ADVANCED
SCIENCE NEWS**

www.advancedsciencenews.com
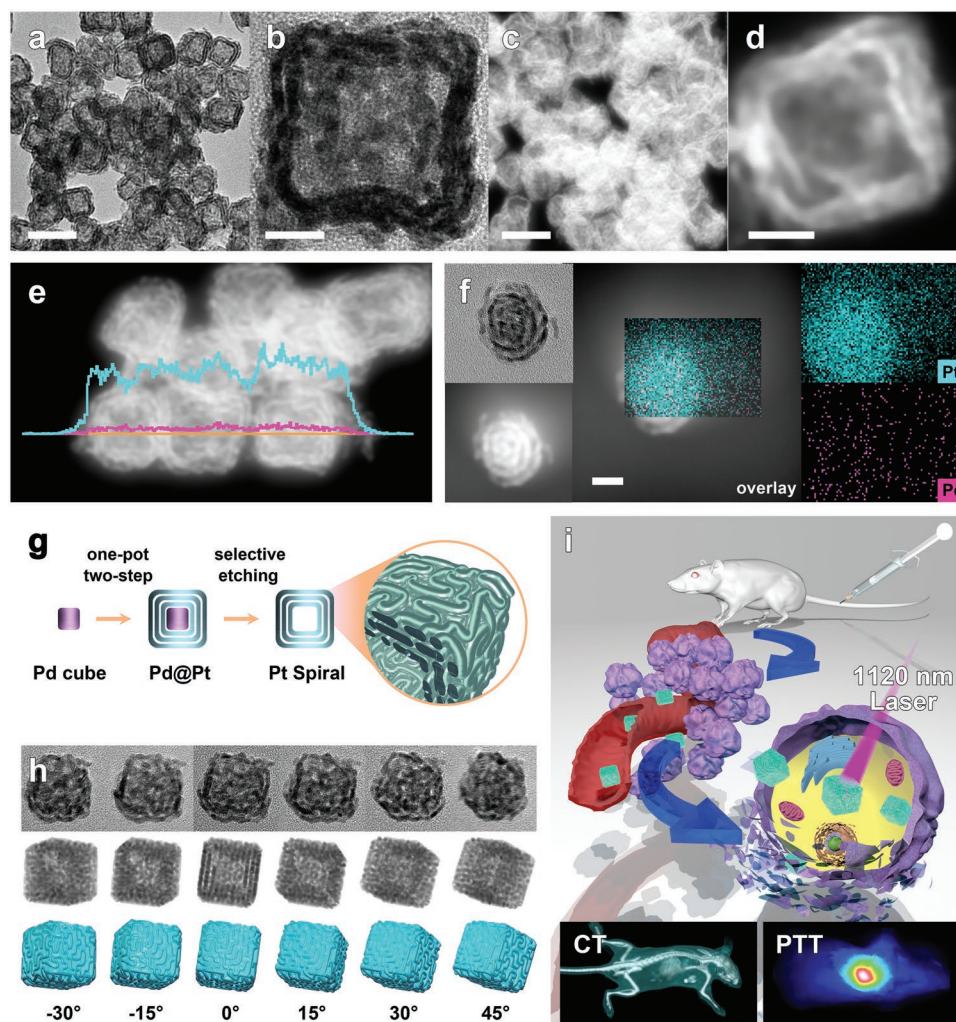
**ADVANCED
MATERIALS**

www.advmat.de

Figure 1. a,b) TEM images and c,d) STEM-HAADF images of Pt Spirals. Scale bar: (a,c) 50 nm; (b,d) 10 nm. e,f) Corresponding STEM-EDX profile (e) and mapping analysis (f) of Pt Spirals: Pt (cyan) and Pd (magenta). Scale bar: 10 nm. g) Schematic illustrations of the formation and the three-level structure of a Pt Spiral. h) Rotational TEM images of Pt Spirals with various angles and corresponding schematic 3D model images rendered as translucent and reflectance textures. i) Schematic illustration of Pt Spirals as theranostic platforms for CT imaging-guided photothermal therapy.

Noble-metal nanostructures have great potential as the photothermal agents owing to their tunable localized surface plasmon resonance (SPR) resulting from the resonant collective oscillation of conduction electrons, and self-thermalization effect resulting from electron–phonon scattering.[33–48] Although regulating the structure, such as shape and size is a well-known strategy to tune the SPR wavelength across the visible and near-infrared spectral range, biological applications of noble metal nanostructures are rarely extended to NIR-II.[1–5] Because the high order longitudinal SPR mode of Pt nanostructures locates in the near-infrared zone,[49–51] it is promising to extend their plasmon wavelengths beyond ≈1000 nm through finely adjusting their structures. Moreover, Pt nanostructures have good biocompatibility and high K-edge value (78.4 keV), offering them great potential for X-ray computed tomography (CT) imaging guided PTT. However, to the best of our knowledge, there are only a few reports to date on the applications of Pt nanostructures compared with that of Au nanostructures in the field of PTT, let alone developing their photothermal therapy effect in NIR-II.

In this study, we design and synthesize unique hollow Pt nanoframes ("Pt Spirals") with multilevel structure by a simple selective etching strategy, which exhibited high extinction coefficients and strong SPR covering both NIR-I and NIR-II biowindows. As shown in transmission electron microscopy (TEM) and scanning transmission electron microscopy (STEM-HAADF) images (**Figure 1**a–d; Figures S1–S3, Supporting Information), uniform hollow cubic nanoframes with an average size of ≈30 nm are formed after the etching process, and no evident size change occurs comparing to as-prepared Pd@Pt templates.[52] The obtained nanoframes exhibit an apparently spiral shape consisting of 2 to 3 layers with an average thickness of 2 nm. Energy-dispersive X-ray analysis (EDX) results of Pt Spiral (Figure 1e,f) suggest Pd cores are removed in the etching process and confirm the hollow structure. Rotational TEM images (Figure 1h) reveal that the Pt layer is composed with Pt nanowires. The apparently spiral shape emerges in specific viewing angles, which is in good compliance with the simulated images. The broken particle in
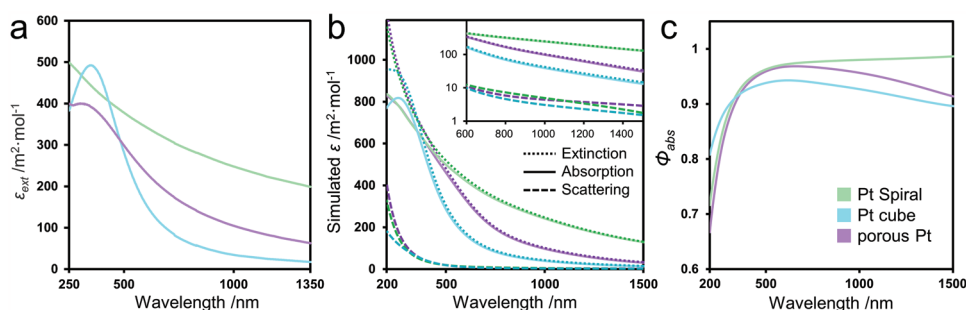
**ADVANCED
SCIENCE NEWS**
www.advancedsciencenews.com

**ADVANCED
MATERIALS**
www.advmat.de

Figure 2. a) Molar extinction coefficient (ε_{ext}) of Pt Spirals, Pt cubes, and porous Pt spheres in aqueous solutions. b) Simulated molar extinction, absorption, and scattering coefficient (ε) and c) simulated adsorption efficiency (Φ_{abs}) of Pt Spirals, Pt cubes, and porous Pt spheres in water. Inset in (b) uses logarithmic coordinate for clearance.

Figure S4 (Supporting Information) clearly shows how 2 nm Pt nanowires and their bifurcations assemble the monocomponent layered superstructure, i.e., 1D nanowires assemble tangentially into 2D shells, and then assemble layer-by-layer into hollow 3D frame superstructure.

Benefited from the unique three-level structure, Pt Spirals have plenty of interfaces, which induce strong SPR. Compared to the solid Pt cubes and superstructured porous Pt dendritic spheres with radial channels, Pt Spirals exhibit strong broad absorption along the entire measured range of 250–1350 nm, indicating their good adsorption properties in both biowindows (Figures S5–S7, Supporting Information). The broadband absorption of Pt Spirals is simulated and proved by finite-difference time-domain (FDTD) approach (Figure S8, Supporting Information). Considering that the SPR mode in Pt depends on the aspect ratio,[50,51] we deduce that the impressive absorption properties could be ascribed to the unique structure assembled by Pt nanowires. Owing to the various aspect ratios of Pt nanowires, the longitudinal SPR broad peaks in near-infrared zone superposed, generating the strong and smooth absorption in near-infrared zone, whereas the transverse mode at ultraviolet zone attributed to the uniform diameter of Pt nanowires.

To quantify the structural influences, molar extinction, absorption, and scattering coefficient (ε) of Pt cubes, porous Pt spheres, and Pt Spirals are calculated and simulated as shown in **Figure 2**a,b. It is demonstrated that the calculated and simulated results have an astonishing resemblance, especially in the near-infrared zone, further illustrating the influence of the superstructure of Pt on extending the adsorption of near-infrared light. Both superstructured Pt nanomaterials have stronger adsorption than solid nanoparticles in the near-infrared zone owing to the better atomic utilization efficiency. At 808 nm in NIR-I, the measured extinction coefficient (ε_{ext}) of Pt Spirals is 4.7 times higher than that of Pt cube. Moreover, the ratio continues to rise as the wavelength increasing. At 1120 nm, the ratio is 8.5, and the highest ratio is up to 11.4 in NIR-II (Figure S9, Supporting Information). The simulation also gives the information of scattering. Both platinum superstructures have outstanding adsorption efficiencies (Φ_{abs}, the ratio of absorption and extinction cross-section, shown in Figure 2c) in the near-infrared zone. For example, only no more than 1.8% photons are scattered at 1120 nm for Pt Spirals, which are much lower than that of porous Pt spheres and Pt cubes (5.1% and 8.0%). Such low scattering could ascribe to the

multilayer structure of Pt Spirals, resulting in that the scattered photons could be occasionally absorbed by the adjacent layer.

Motivated by the good adsorption properties, the photothermal performances of Pt Spirals in NIR-II are further investigated employing 1120 nm laser as representative excitation light. As shown in **Figure 3**a–d, the temperature variation depends on both the concentrations of Pt Spirals and the power density of the 1120 nm laser. In contrast to the water, the temperature of Pt Spirals (100 µg mL^{-1}) increases to 53.1 °C within 1000 s at a power of 1.2 W, and the ΔT_{max} (equilibrium temperature vs ambient temperature of the surroundings) is over 20 °C even at the low concentration of 25 µg mL^{-1}, indicating a highly efficient photothermal effect. PCE (η) of Pt Spirals is high at 52.5% (calculation details in Figure S10, Supporting Information), which is much higher than those of Pt cubes (32.3%) and porous Pt (43.2%). Importantly, it is the highest for reported platinum nanoagents in NIR-II to date (22.98–38.9%; see Table S1, Supporting Information). Such good photothermal performances further validate the structural advantages of Pt Spirals. The aging test, photostability test, and the extreme test of Pt Spirals in high-boiling-point solvent *N,N*-dimethyl formamide demonstrate the excellent stability, strong photothermal effect, and superb heat-resistance properties of Pt Spirals (Figure 3e; Figures S11–S14, Supporting Information).

For investigating the structural influence on PCE, FDTD simulations, and density functional theory (DFT) simulations are performed to show the electric field enhancement (denoted as $|E|/|E_0|$, the ratio of enhanced electric field to incident one) and hot electron generation. As shown in Figure 3g, although Pt Spirals exhibit higher electric field enhancement than porous Pt, the strongest $|E_{max}|/|E_0|$ appears in bare Pt cube. DFT results (Figure 3f; Figure S15, Supporting Information) suggest that the dimer structure selected for simulating the superstructure decreases the system energy after ionization and promotes the hot electrons separating from the cavities and escaping. The weak correlation between PCE and the electric field enhancement demonstrates that the efficiency could not be entirely determined by the enhancement. Coincidentally, the similar phenomenon that plasmonic nanoparticles with superstructure exhibit weaker electric field enhancement but superior properties to solid structures is also observed by other researchers.[33] Furthermore, the electric field enhancement is determined to dominate the amount of hot electrons.[43,53] A probable energy transfer process in Pt Spirals can be drawn that the hot
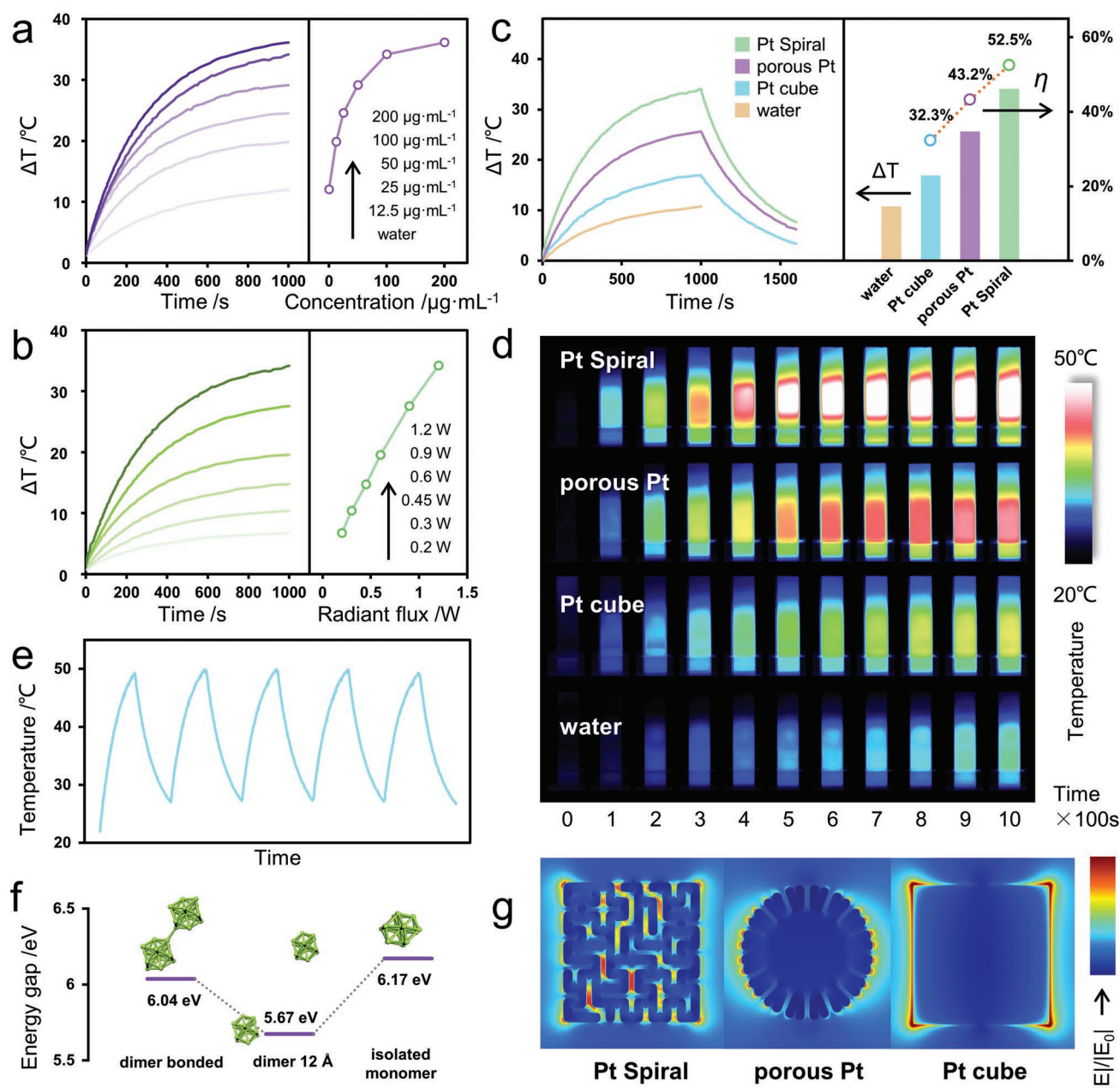
Figure 3. a,b) Temperature rising curves and temperature difference (ΔT) of Pt Spirals with various concentrations (a) and radiant fluxes (b). c) Temperature rising-decay curves, temperature difference (ΔT), photothermal conversion efficiencies (η), and d) relative infrared thermal images of Pt Spirals, porous Pt spheres, and Pt cubes. e) Cyclical photothermal test of Pt Spirals. The experiments in (a)–(e) are carried out with 2 mL aqueous solution with a concentration of 100 µg mL^{-1} under 1120 nm irradiation at a power of 1.2 W, unless otherwise specified. The cyclical photothermal test in (e) is repeated five times with irradiation for 600 s and then shutting off for the same period in each on/off cycle. f) Simulated system energy gap in dimer structure. g) Electric field enhancement distributions of Pt Spiral, porous Pt sphere, and Pt cube at 1120 nm excitation.

electrons acquire energy from photons, then with effective separation, and finally dissipate to phonons in nonradiation process. The excitation and the separation processes synergistically influence PCE. Thus, the superstructure of Pt Spirals is the significant cause for its excellent photothermal performance.

To improve their biocompatibility, polyethylene glycol thiol (PEG-SH) has been successfully modified on the surface of Pt Spirals, proved by the significant change of zeta potential. The

obtained nanoagents maintained the good adsorption and photothermal stabilities in biological medium (Figures S16–S19, Supporting Information). Prior to the further biological applications of Pt Spirals, the biocompatibility is evaluated by a traditional CCK-8 assay using the human cervix cancer cell line (HeLa) and the mouse mammary tumor cell line (4T1). As shown in Figure S20 (Supporting Information), the viabilities are higher than 89.5% for both HeLa and 4T1 cells at the
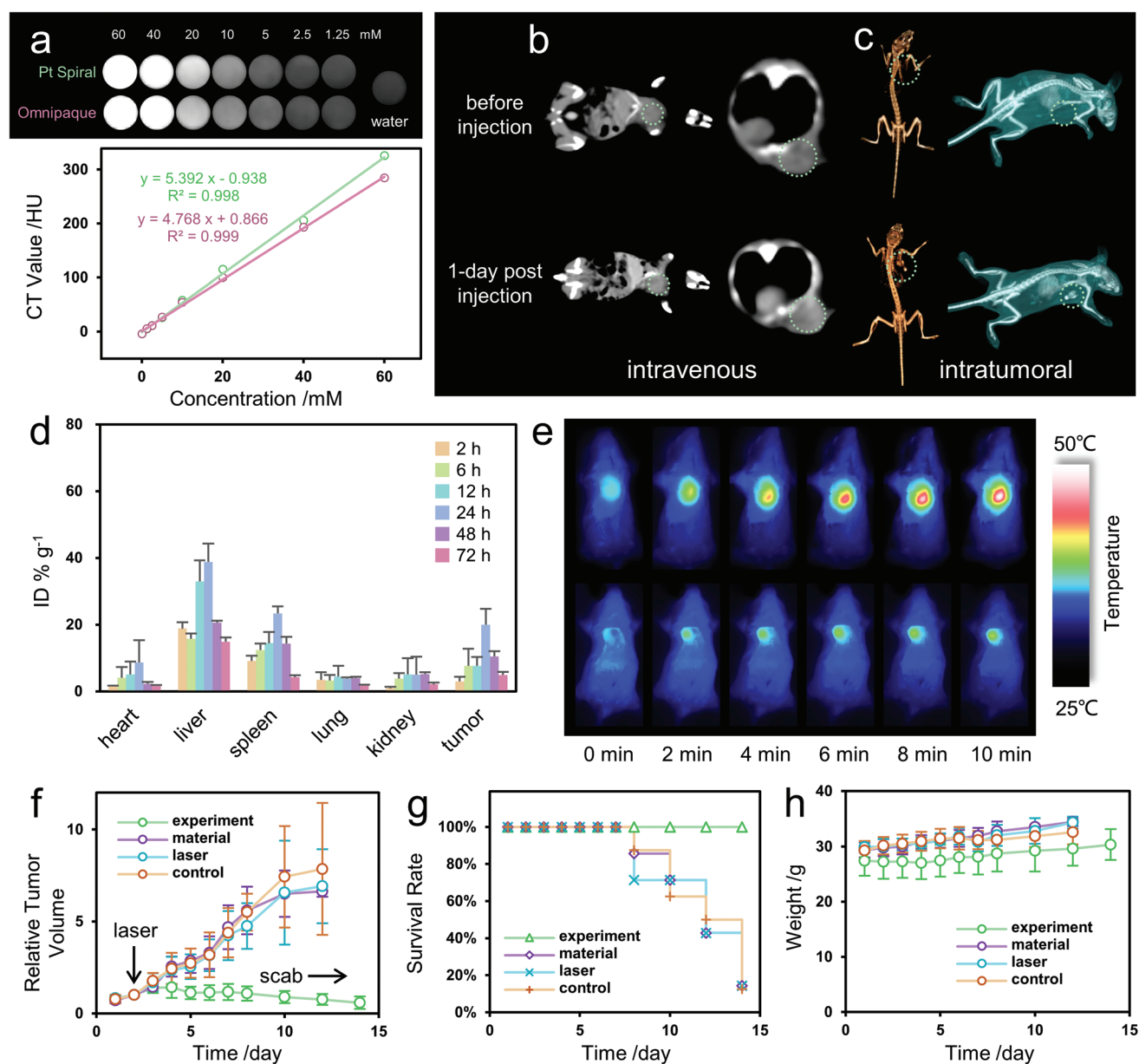
Figure 4. a) In vitro CT images and CT value as a function of the concentration of Pt Spirals and Omnipaque. b,c) In vivo CT images of a tumor-bearing mouse: b) CT cross-section and longitudinal section images taken before and post intravenous injection of Pt Spirals, c) CT tomographic reconstruction images of before and post intratumoral injection of Pt Spirals. d) Time-dependent in vivo distribution of platinum in tumor-bearing mice. e) Infrared thermal images of tumor-bearing mice irradiated with 1120 nm laser (0.5 W cm^{-2}). f) Relative tumor volume, g) survival rate, and h) weight of tumor-bearing mice from different groups after various treatments, counting survival mice only.

concentration of 20 µg mL^{-1} after the incubation for 24 h, which shows good biocompatibility without significant cytotoxicity. For the anticancer effect, the cell viability significantly decreases when increasing the concentration of Pt Spirals after irradiating with a beam of 1120 nm laser for 10 min at 0.5 W cm^{-2}. The hyperthermia inducing apoptosis of tumor cells in a matter of minutes, indicating remarkable PTT effect. These results demonstrate that Pt Spirals are promising for highly effective PTT for cancer.

Due to the strong X-ray attenuation of Pt, we further access the potential of Pt Spirals as CT contrasts for tumor diagnosis.

As shown in **Figure 4**a, Pt Spirals exhibited higher contrast efficacy than that of commercial iodine-containing agent (Omnipaque) at equivalent concentrations, which could be attributed to their high K-edge value. To verify the imaging effect in vivo, mice bearing U14 tumors are intravenously or intratumorally injected with Pt Spirals and then imaged by a CT scanner (Figure 4b,c; Figure S21, Supporting Information). The remarkable enhancement of CT signals in tumor position is detected after 24 h post intravenous injection, indicating the enhanced permeability and the retention effect of Pt Spirals in tumor. After intratumoral injection, the tumor is clearly presented in

**ADVANCED
SCIENCE NEWS**

www.advancedsciencenews.com

**ADVANCED
MATERIALS**

www.advmat.de

the CT tomographic reconstruction images. The CT results suggest Pt Spirals could act as powerful candidates for tumor imaging.

The blood circulation time and in vivo distribution experiments of Pt Spirals are investigated by intravenous injection and ICP for determining the Pt concentration. The half-time of the blood circulation is estimated to be 2.91 ± 0.51 h (Figure S22, Supporting Information), allowing the enrichment of Pt Spirals in tumors. Meanwhile, the major organs (including heart, liver, spleen, lung, and kidney) and tumors are collected at various times post injection (Figure 4d). The results show that Pt Spirals mainly accumulate in the liver, matching the approach of the mononuclear phagocyte system,[31] and accumulate by the tumor cells through the enhanced permeability and retention.[54] The analysis also reveals that the accumulation of Pt Spirals in tumors reaches a maximum at 24 h post injection, providing more information for the optimal treatment time. Encouraged by the good antitumor effect in vitro, the PTT effect in vivo is further studied using the mouse U14 cancer xenograft model. The mice are randomly divided into four groups and intravenously injected with 0.66 mg kg^{-1} Pt Spirals (experiment and material groups) and 0.9% NaCl aqueous solution (laser and control groups) on the first day. At 24 h post injection, the tumor areas of the mice in the experiment and laser groups are irradiated by 1120 nm laser (0.5 W cm^{-2}, lower than MPE: 1 W cm^{-2}) for 10 min. During the laser irradiation, the skin temperature is monitored by an infrared thermal camera (Figure 4e). In contrast to the laser group of 41.9 °C, the experiment group reaches an average value of 49.9 °C of the highest skin temperature at the tumor position after 10 min of irradiation. The hyperthermia could cause unfolding of proteins in short time, leading irreversible damage to cancer cells. Normal tissues outside the irradiation area maintain a quite low temperature (around 40 °C), which may cause cell inactivation (if lasting several hours) but is not irreversible.[55] The tumor sizes and survival rate are then recorded (Figure 4f,g; Figures S23 and S24, Supporting Information). In the experiment group, in spite of the slight increase in tumor volumes observed over the next two days, the lesions of hyperthermia emerge from the interior of the tumors and induce bruising and then scarring at the same time. The tumors gradually shrink, and then the scabs gradually vanish ten days after the irradiation. The tumors are almost eliminated and all mice survive after the experimental period. By contrast, tumors in the other three groups grow rapidly. The hematoxylin–eosin (H&E) staining images of tumors show necrosis in the experiment group (Figure S25, Supporting Information), suggesting that neither laser-only nor material-only could prevent the tumor growth. The body weight of mice in all groups shows no obvious variation, indicating few influences of PTT on mice. In addition, the insignificant cytotoxicity of Pt Spirals is also confirmed by the H&E staining images of the major organs and the blood analysis in experiment and control groups (Figures S26 and 27, Supporting Information). These positive results demonstrate that Pt Spirals with good biocompatibility are promising for ablating tumors without recurrence using the light in NIR-II at the safe power density in vivo.

In summary, we have successfully developed a Pt superstructure assembled at three levels (3D frame, 2D layered shells, and 1D nanowires), which exhibits high PCE (52.5%) and molar extinction coefficient (228.7 m^2 mol^{-1}) in NIR-II. The outstanding photothermal properties are proved by the FDTD and DFT simulations, which indicate that the excitation and separation processes of hot electrons synergistically influence PCE. Obviously, the superstructure of Pt Spirals is the significant cause of its excellent photothermal performance. Most importantly, PCE of Pt Spirals is also significantly higher than that of reported platinum nanoagents in NIR-II, resulting in the outstanding photothermal effect in vitro and in vivo. Superb heat-resistance properties, excellent photostability, good biocompatibility, effective tumor imaging, and anticancer effects afford Pt Spirals great potential as effective theranostic platforms for CT imaging-guided photothermal therapy. Moreover, from solid nanoparticles to superstructures, adsorption and photothermal properties are boosted at the same time within the monocomponent without any tradeoff, which provides insight for further developing high-performance theranostic materials through structural design and SPR tuning. We hope that the results are also informative for other field, such as photocatalyst, plasmon-based sensors and devices.

Supporting Information

Supporting Information is available from the Wiley Online Library or from the author.

Conflict of Interest

The authors declare no conflict of interest.

[1] K. Cai, W. Zhang, J. Zhang, H. Li, H. Han, T. Zhai, *ACS Appl. Mater. Interfaces* **2018**, *10*, 36703.

[2] J. Zhou, Y. Jiang, S. Hou, P. K. Upputuri, D. Wu, J. Li, P. Wang, X. Zhen, M. Pramanik, K. Pu, H. Duan, *ACS Nano* **2018**, *12*, 2643.

[3] M. Ji, M. Xu, W. Zhang, Z. Yang, L. Huang, J. Liu, Y. Zhang, L. Gu, Y. Yu, W. Hao, P. An, L. Zheng, H. Zhu, J. Zhang, *Adv. Mater.* **2016**, *28*, 3094.

[4] Y. Tang, T. Yang, Q. Wang, X. Lv, X. Song, H. Ke, Z. Guo, X. Huang, J. Hu, Z. Li, P. Yang, X. Yang, H. Chen, *Biomaterials* **2018**, *154*, 248.

[5] P. Vijayaraghavan, C.-H. Liu, R. Vankayala, C.-S. Chiang, K. C. Hwang, *Adv. Mater.* **2014**, *26*, 6689.

[6] Z. Yin, W. Zhang, Q. Fu, H. Yue, W. Wei, P. Tang, W. Li, W. Li, L. Lin, G. Ma, D. Ma, *Small* **2014**, *10*, 3619.

[7] X. Cheng, R. Sun, L. Yin, Z. Chai, H. Shi, M. Gao, *Adv. Mater.* **2017**, *29*, 1604894.

[8] D. Y. Lee, J. Y. Kim, Y. Lee, S. Lee, W. Miao, H. S. Kim, J.-J. Min, S. Jon, *Angew. Chem.* **2017**, *129*, 13872.

[9] M. Manikandan, N. Hasan, H.-F. Wu, *Biomaterials* **2013**, *34*, 5833.

[10] Q. Ma, L. Cheng, F. Gong, Z. Dong, C. Liang, M. Wang, L. Feng, Y. Li, Z. Liu, C. Li, L. He, *J. Mater. Chem. B* **2018**, *6*, 5069.

[11] Y. Chen, P. Han, Y. Wu, Z. Zhang, Y. Yue, W. Li, M. Chu, *Small* **2018**, *14*, 1802799.

[12] C. Liu, L. Luo, L. Zeng, J. Xing, Y. Xia, S. Sun, L. Zhang, Z. Yu, J. Yao, Z. Yu, O. U. Akakuru, M. Saeed, A. Wu, *Small* **2018**, *14*, 1801851.

[13] P. Lei, R. An, P. Zhang, S. Yao, S. Song, L. Dong, X. Xu, K. Du, J. Feng, H. Zhang, *Adv. Funct. Mater.* **2017**, *27*, 1702018.

[14] W. Zhen, Y. Liu, L. Lin, J. Bai, X. Jia, H. Tian, X. Jiang, *Angew. Chem., Int. Ed.* **2018**, *57*, 10309.

[15] M. Wang, K. Deng, W. Lü, X. Deng, K. Li, Y. Shi, B. Ding, Z. Cheng, B. Xing, G. Han, Z. Hou, J. Lin, *Adv. Mater.* **2018**, *30*, 1706747.

[16] X. Song, H. Gong, S. Yin, L. Cheng, C. Wang, Z. Li, Y. Li, X. Wang, G. Liu, Z. Liu, *Adv. Funct. Mater.* **2014**, *24*, 1194.

[17] C. Yao, W. Wang, P. Wang, M. Zhao, X. Li, F. Zhang, *Adv. Mater.* **2018**, *30*, 1704833.

[18] B. Ding, C. Yu, C. Li, X. Deng, J. Ding, Z. Cheng, B. Xing, P. Ma, J. Lin, *Nanoscale* **2017**, *9*, 16937.

[19] T. Liu, C. Wang, X. Gu, H. Gong, L. Cheng, X. Shi, L. Feng, B. Sun, Z. Liu, *Adv. Mater.* **2014**, *26*, 3433.

[20] V. Yadav, S. Roy, P. Singh, Z. Khan, A. Jaiswal, *Small* **2019**, *15*, 1803706.

[21] P. Wang, Y. Shi, S. Zhang, X. Huang, J. Zhang, Y. Zhang, W. Si, X. Dong, *Small* **2019**, *15*, 1803791.

[22] L. Sun, Z. Li, R. Su, Y. Wang, Z. Li, B. Du, Y. Sun, P. Guan, F. Besenbacher, M. Yu, *Angew. Chem., Int. Ed.* **2018**, *57*, 10666.

[23] Z. Tang, H. Zhang, Y. Liu, D. Ni, H. Zhang, J. Zhang, Z. Yao, M. He, J. Shi, W. Bu, *Adv. Mater.* **2017**, *29*, 1701683.

[24] Q. Xiao, X. Zheng, W. Bu, W. Ge, S. Zhang, F. Chen, H. Xing, Q. Ren, W. Fan, K. Zhao, Y. Hua, J. Shi, *J. Am. Chem. Soc.* **2013**, *135*, 13041.

[25] Y. Wang, H. Wang, D. Liu, S. Song, X. Wang, H. Zhang, *Biomaterials* **2013**, *34*, 7715.

[26] J. Liu, C. Wang, X. Wang, X. Wang, L. Cheng, Y. Li, Z. Liu, *Adv. Funct. Mater.* **2015**, *25*, 384.

[27] J. Du, N. Xu, J. Fan, W. Sun, X. Peng, *Small* **2019**, *15*, 1805087.

[28] W. Chen, J. Liu, Y. Wang, C. Jiang, B. Yu, Z. Sun, L. Lu, *Angew. Chem., Int. Ed.* **2019**, *58*, 6290.

[29] M. Abbas, Q. Zou, S. Li, X. Yan, *Adv. Mater.* **2017**, *29*, 1605021.

[30] Q. Zou, M. Abbas, L. Zhao, S. Li, G. Shen, X. Yan, *J. Am. Chem. Soc.* **2017**, *139*, 1921.

[31] R. Xing, Q. Zou, C. Yuan, L. Zhao, R. Chang, X. Yan, *Adv. Mater.* **2019**, *31*, 1900822.

[32] Y. Liu, W. Zhen, Y. Wang, J. Liu, L. Jin, T. Zhang, S. Zhang, Y. Zhao, S. Song, C. Li, J. Zhu, Y. Yang, H. Zhang, *Angew. Chem., Int. Ed.* **2019**, *58*, 2407.

[33] J. Guo, Y. Zhang, L. Shi, Y. Zhu, M. F. Mideksa, K. Hou, W. Zhao, D. Wang, M. Zhao, X. Zhang, J. Lv, J. Zhang, X. Wang, Z. Tang, *J. Am. Chem. Soc.* **2017**, *139*, 17964.

[34] M.-F. Tsai, S.-H. G. Chang, F.-Y. Cheng, V. Shanmugam, Y.-S. Cheng, C.-H. Su, C.-S. Yeh, *ACS Nano* **2013**, *7*, 5330.

[35] T. J. Norman, C. D. Grant, D. Magana, J. Z. Zhang, J. Liu, D. Cao, F. Bridges, A. Van Buuren, *J. Phys. Chem. B* **2002**, *106*, 7005.

[36] S. Eustis, M. A. El-Sayed, *Chem. Soc. Rev.* **2006**, *35*, 209.

[37] S. Link, C. Burda, M. B. Mohamed, B. Nikoobakht, M. A. El-Sayed, *Phys. Rev. B* **2000**, *61*, 6086.

[38] H. Wang, N. J. Halas, *Adv. Mater.* **2008**, *20*, 820.

[39] L. V. Besteiro, X.-T. Kong, Z. Wang, G. Hartland, A. O. Govorov, *ACS Photonics* **2017**, *4*, 2759.

[40] G. Baffou, R. Quidant, F. J. García de Abajo, *ACS Nano* **2010**, *4*, 709.

[41] M. Sun, L. Xu, W. Ma, X. Wu, H. Kuang, L. Wang, C. Xu, *Adv. Mater.* **2016**, *28*, 898.

[42] Z. Yin, Y. Wang, C. Song, L. Zheng, N. Ma, X. Liu, S. Li, L. Lin, M. Li, Y. Xu, W. Li, G. Hu, Z. Fang, D. Ma, *J. Am. Chem. Soc.* **2018**, *140*, 864.

[43] S. Linic, U. Aslam, C. Boerigter, M. Morabito, *Nat. Mater.* **2015**, *14*, 567.

[44] E. Cortés, W. Xie, J. Cambiasso, A. S. Jermyn, R. Sundararaman, P. Narang, S. Schlücker, S. A. Maier, *Nat. Commun.* **2017**, *8*, 14880.

[45] R. Jin, Y. C. Cao, E. Hao, G. S. Métraux, G. C. Schatz, C. A. Mirkin, *Nature* **2003**, *425*, 487.

[46] J. A. Scholl, A. L. Koh, J. A. Dionne, *Nature* **2012**, *483*, 421.

[47] Y.-Z. Chen, Z. U. Wang, H. Wang, J. Lu, S.-H. Yu, H.-L. Jiang, *J. Am. Chem. Soc.* **2017**, *139*, 2035.

[48] S. Link, M. A. El-Sayed, *J. Phys. Chem. B* **1999**, *103*, 8410.

[49] J. A. Creighton, D. G. Eadon, *J. Chem. Soc., Faraday Trans.* **1991**, *87*, 3881.

[50] N. Zhang, C. Han, Y.-J. Xu, J. J. F. Iv, D. Zhang, J. Codrington, S. K. Gray, Y. Sun, *Nat. Photonics* **2016**, *10*, 473.

[51] S. Jung, K. L. Shuford, S. Park, *J. Phys. Chem. C* **2011**, *115*, 19049.

[52] Q. Wang, J. Li, X. Wang, Y. Liu, Y. Long, J. Li, J. Pan, S. Song, H. Zhang, *Chem. - Eur. J.* **2018**, *24*, 15649.

[53] A. Manjavacas, J. G. Liu, V. Kulkarni, P. Nordlander, *ACS Nano* **2014**, *8*, 7630.

[54] Y. Liu, W. Zhen, Y. Wang, J. Liu, L. Jin, T. Zhang, S. Zhang, Y. Zhao, N. Yin, R. Niu, S. Song, L. Zhang, H. Zhang, *Nano Lett.* **2019**, *19*, 5093.

[55] D. Jaque, L. M. Maestro, B. del Rosal, P. Haro-Gonzalez, A. Benayas, J. L. Plaza, E. M. Rodríguez, J. G. Solé, *Nanoscale* **2014**, *6*, 9494.

1904836 (7 of 7)